

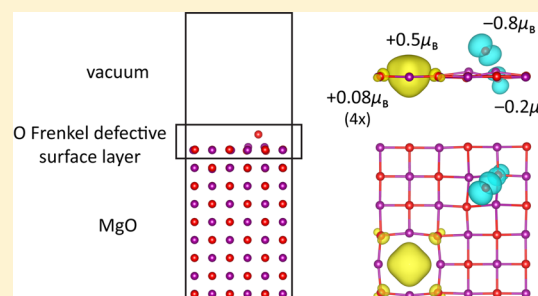
Structural and Electronic Properties of Frenkel and Schottky Defects at the MgO{100} Surface: Spin Polarization, Mid-Band Gap States, and Charge Trapping at Vacancy Sites

Heleen van Gog* and Marijn A. van Huis^{1b}

Soft Condensed Matter, Debye Institute for Nanomaterials Science, Utrecht University, Princetonplein 5, 3584 CC Utrecht, The Netherlands

S Supporting Information

ABSTRACT: Recent experimental and simulation studies on the hydration of MgO suggest that physically and chemically induced surface defects strongly promote the reaction. The results of density functional theory calculations on the stability and the structural and electronic properties of Frenkel and Schottky defects at the MgO{100} surface performed in light of the surface chemistry of MgO are presented here. Comparison of calculated formation energies shows that Frenkel and Schottky defects are more likely to be formed at the surface than in the bulk. Frenkel adatoms were found to induce a strong local restructuring of surface atoms. The lowest energy configurations include spin-polarized and dumbbell-type reconstructions for Mg and O Frenkel adatoms. O Frenkel vacancies were observed to trap significant amounts of electronic charge. Analysis of the electronic density of states reveals that surface Frenkel defects introduce many electronic defect states in the wide band gap of perfect MgO. These findings are a strong indication that the defective MgO surface is not chemically inert and will more easily bind or dissociate molecules and ions.



INTRODUCTION

MgO is a ceramic material of wide-ranging importance in physics, geophysics, chemistry, and technology. In its surface chemical activity, a key role is played by structural defects. Previous experimental and simulation studies on the interaction of water with the surface of MgO, for example, have shown that while the defect-free MgO{100} surface is extremely inert toward hydroxylation and further hydration when exposed to water, the surface interaction of MgO with water can be strongly enhanced by physically or chemically inducing surface defects (see refs.^{1–3} and references cited therein). Most experimental work can only reveal the properties of extended surface defects. Recent experimental studies, however, suggest that point defects play an important role in the activation of MgO as well: in a synchrotron-based photoemission spectroscopy study of the reaction of water vapor at partial pressures $\leq 2.0 \times 10^{-5}$ Torr with vacuum-cleaved MgO{100} surfaces, Liu et al. found that the hydroxyl coverage of the surface increases from approximately 5% for a clean flat surface to approximately 35% for an Ar⁺-sputtered surface;⁴ and investigating MgO smoke nanocrystals under partial pressures of water ranging from 10 mTorr to 10 Torr using environmental transmission electron microscopy (ETEM), Gajdardziska-Josifovska et al. found the hydroxide formation to be electron beam-driven, the reaction taking place only in areas irradiated with high energy electrons while exposed to water, and the reaction rate increasing with the electron flux.⁵

The increase in the reaction rate constant due to electron beam irradiation has been quantified for the dissolution of metal oxides in water by Lu et al.⁶ Enhanced dissolution in a liquid environmental transmission electron microscope (LETEM) was efficiently utilized in that study for the high precision patterning of various metal oxide films in water, i.e., an eco-friendly electron lithography method. The mechanism of electron beam etching of metal oxides has been investigated by Shen et al., who, using in situ high-resolution transmission electron microscopy (HRTEM), recorded the atom by atom etching of CaO crystals.⁷ Readsorption (as adatoms) of some of the sputtered atoms was found to be a part of the etching process in that study. Electron beam etching methods hold great promise for nanostructuring with single-atom precision. The possibility of engineering the defining features of nanodevices at the atomic scale underlines the importance of understanding the properties of point defects such as adatoms and vacancies, and combinations thereof, at the surface of materials.

There have been numerous computational studies on MgO surface defects. Apart from Frenkel and Schottky defects,^{8–11} which are the topic of our study and of which we will discuss the available literature into more detail below, calculations have been performed on terrace steps or edges,¹² O and Mg

Received: February 27, 2019

Revised: May 11, 2019

Published: May 22, 2019

monovacancies,^{12–15} adatoms,¹⁶ dopants,^{15,17} and on the adsorption of molecular species onto particular surface defects.^{15,17,18} The presence of defects is strongly related to the overall electronic structure of an MgO material, as has been shown by Richter et al., who investigated the influence of doping on the formation energy and concentration of O surface vacancies through a combination of computational methodologies,¹⁴ and by Uchino and Yoko, who investigated point defects in nanoscale blocks of MgO and found a collection of spin-polarized states depending on the presence and distribution of Mg vacancies.¹⁹ A recent example of a molecule adsorption study on MgO surface defects is the work by Alvim et al., who investigated proton migration on perfect, vacancy-defected, and Al-doped MgO(001) surfaces.¹⁵

The recent experimental developments discussed above show that surface defects which are a combination of point defects are a most relevant topic of research. Stoichiometric surface point defects that are a combination of vacancies and adatoms are the subject of this paper. We investigated the structural and electronic properties of Frenkel and Schottky defects at the MgO{100} surface. Using plane-wave density functional theory (DFT) calculations, and taking into account the possibility of spin-polarized solutions, we calculated the formation energy and structural properties of lower energy configurations. To study the electronic properties, an analysis of the electronic density of states (DOS) and charge distribution was carried out. For Mg Frenkel defects at the MgO{100} surface, no previous calculations were found in the literature. O Frenkel defects at the MgO{100} surface have been investigated before: two studies report results, one by Di Valentin et al., who, using a DFT cluster model approach, considered nonmagnetic solutions only,⁸ and the other by Ménétrey et al., who used plane-wave DFT to study both spin-polarized and unpolarized configurations and reported a magnetic solution to be the lowest energy configuration.⁹ Our results show that the magnetic configuration reported by the latter study is not the lowest energy configuration for the surface O Frenkel defect: we identified two lowest energy configurations that are lower in energy. The Schottky defect at the MgO{100} surface has also been investigated before: Ojamäe and Pisani report formation energies and structural properties obtained using a Hartree–Fock approach,¹⁰ and Antoshchenkova et al. studied the Schottky surface defect using molecular dynamics and DFT simulations.¹¹ There have been many simulation studies of bulk MgO Frenkel and Schottky defects (see refs,^{11,20} and references cited therein). We studied the Frenkel and Schottky defects in the MgO bulk as well to compare the MgO{100} surface defects with their bulk counterparts.

METHODOLOGY

Computational Methods. The DFT calculations were carried out using the first-principles Vienna Ab initio Simulation Package (VASP).^{21–23} Within the projector-augmented wave framework,^{24,25} the Perdew–Burke–Ernzerhof (PBE) generalized gradient approximation functional²⁶ was employed for the exchange and correlation energy terms. The cutoff energy of the wave functions was set to 750 eV, and the cutoff energy of the augmentation functions was set to 1050 eV. The electronic wave functions were sampled, using the Monkhorst and Pack scheme,²⁷ on $4 \times 4 \times 4$ k -grids for bulk supercells and on $4 \times 4 \times 1$ k -grids for surface supercells: The bulk defect calculations were performed on $3a_0 \times 3a_0 \times 3a_0$

supercells, a_0 being the MgO lattice constant, and the perfect cell containing 216 atoms. For the {100} surface defect calculations, $3a_0 \times 3a_0$ habit plane supercells were constructed, each consisting of a nine atomic layers high MgO slab and a 15 Å high vacuum slab, with 324 atoms in the perfect configuration. The cutoff energies of the electronic wave and augmentation functions and the density of the k -grids were tested to ensure energy convergence well within 2 meV/atom.

Bulk Frenkel defects were simulated by displacing one atom within the perfect bulk supercell to an interstitial site located as far as possible from the displaced atom's original site. Three different starting configurations were considered, as can be found illustrated in Figure S1a–c in the [Supporting Information](#): one with the interstitial atom at the octahedral site at the center of a cube of atoms; one with the interstitial atom closer, at a distance of $\frac{1}{8}\sqrt{3}a_0$ from one of the lattice atoms; and one with the interstitial atom at a distance of $\frac{1}{4}\sqrt{3}a_0$ from one of the lattice atoms, displaced to create a lattice site centered dumbbell. Supercells containing bulk Schottky defects were obtained by creating one Mg vacancy and one O vacancy within the perfect supercell, resulting in Schottky pairs when separating the vacancies as far as possible and in Schottky dimers (divacancies) when creating the vacancies at adjacent sites.

Surface Frenkel defects were investigated, starting from four different input configurations for unpolarized defects and using eight different input configurations for spin-polarized defects, with surface adatoms displaced as far away as possible from the surface vacancy site. [Figure S1d–g](#) illustrates the different starting positions that were considered for the Frenkel adatoms: on top of a surface O atom (“top-O” site), on top of a surface Mg atom (“top-Mg” site), at a position bridging adjacent surface Mg and O atoms (“bridge” site), or on top of the center of the square defined by four surface atoms (“square” site); placing the adatom at a distance of $1/4 a_0$ normal to the surface layer when performing unpolarized calculations; and considering distances for the adatom of $1/4 a_0$ and $1/2 a_0$ normal to the surface layer when performing spin-polarized calculations. The surface Schottky pair and dimer defects were simulated by removal of one Mg and one O atom from the surface layer.

All simulation cells were structurally optimized, relaxing atomic positions and lattice parameters, to yield lower energy configurations. Accumulative energy and atomic force convergence criteria of 10^{-4} eV and 0.01 eV/Å, respectively, were applied for the ionic relaxation loop and an energy convergence criterium of 10^{-6} eV for the electronic convergence loop. For the spin-polarized calculations, which were carried out for Frenkel defective surface configurations only, the initial magnetic moment was set to $2 \mu_B$ for all Mg atoms within the supercell when simulating the Mg surface Frenkel defect and to all O atoms within the supercell when simulating the O surface Frenkel defect. The magnetic moments were not fixed but allowed to relax during the electronic self-consistent calculation. This starting setting for the magnetic moments served to not only allow spin polarization of the electron density at the adatom, but also allow spin polarization of electron density at vacancy sites; because it is not possible to assign charge nor magnetic moment to a vacancy in its starting configuration, a vacancy's charge and spin polarization have to be “deducted” from adjacent atoms during the electronic self-consistent calcu-

lations. As expected, the magnetic moments on nearly all bulk atoms relaxed to zero during the calculations, and only at and around the adatoms and in and around the vacancy sites, low and high levels of spin polarization were found to remain in a number of cases.

To study the charge distribution among the atoms, a Bader charge analysis²⁸ was carried out using the approach by Henkelman et al.^{29–32} The same approach was used for the evaluation of the magnetic moments on the atoms in spin-polarized defect configurations. All calculations are valid for a temperature of 0 K and a pressure of 0 Pa. Zero-point vibration contributions have been neglected. Noncollinear magnetism has not been considered.

Definition of Defect Formation Energy. The general formula for the formation energy of a defect is³³

$$E_{\text{defect}}^{\text{form}} = E_{\text{defect}}^{\text{total}} - E_{\text{perfect}}^{\text{total}} - \sum_i \Delta n_i \mu_i + q \epsilon_F \quad (1)$$

where $E_{\text{defect}}^{\text{form}}$ is the formation energy of the defect, $E_{\text{defect}}^{\text{total}}$ is the total energy of the defect cell, and $E_{\text{perfect}}^{\text{total}}$ is the total energy of the perfect cell; Δn_i is the number of atoms of species i added to ($\Delta n_i > 0$) or subtracted from ($\Delta n_i < 0$) the perfect cell to obtain the defect cell; μ_i is the atomic chemical potential for these atoms; q is the charge of the defect; and ϵ_F is the Fermi energy. For the calculations performed here, the last term in this equation vanishes ($q = 0$) as Schottky and Frenkel defects can be considered charge-neutral because of the fact that they can be created in MgO bulk crystals without affecting the overall charge state. For Frenkel defects, $\Delta n_{\text{Mg}} = \Delta n_{\text{O}} = 0$, and the second last term vanishes as well. We mention here that single point defects such as isolated adatoms and isolated vacancies and any other nonstoichiometric defects in general cannot be assumed to be uncharged. In such cases, typically electrons have to be manually added to or removed from the total electronic configuration ($q \neq 0$) to evaluate various charge states, and the calculation of the defect formation energy then requires inclusion of thermodynamic corrections as well.^{14,34}

Schottky defects are introduced by removal of one Mg and one O atom. Therefore, for Schottky defects, $\Delta n_{\text{Mg}} = \Delta n_{\text{O}} = -1$. The chemical potentials μ_{Mg} and μ_{O} will differ for atoms belonging to the bulk and the $\{100\}$ surface. Here, the value calculated as $\mu_{\text{Mg}} + \mu_{\text{O}} = 1/N E(\text{Mg}_N\text{O}_N)$ from the total energy of the perfect bulk simulation cell containing N MgO units will be used for all cells. For Frenkel defect supercells containing m MgO pairs, the formation energies of the Frenkel defects are then evaluated by

$$E_{\text{Frenkel}}^{\text{form}} = E_{\text{Frenkel}}^{\text{bulk/surf}}(\text{Mg}_m\text{O}_m) - E_{\text{perfect}}^{\text{bulk/surf}}(\text{Mg}_m\text{O}_m) \quad (2)$$

and for Schottky defect supercells containing $m - 1$ MgO pairs, the formation energies of the Schottky defects by

$$E_{\text{Schottky}}^{\text{form}} = E_{\text{Schottky}}^{\text{bulk/surf}}(\text{Mg}_{m-1}\text{O}_{m-1}) - E_{\text{perfect}}^{\text{bulk/surf}}(\text{Mg}_m\text{O}_m) + \frac{1}{N} E_{\text{perfect}}^{\text{bulk}}(\text{Mg}_N\text{O}_N) \quad (3)$$

where the total energy of the perfect supercell from which the defect supercell was obtained is subtracted from the total energy of the defective supercell, and the energy of one bulk MgO pair is added for Schottky defects.

RESULTS AND DISCUSSION

Bulk Defect Configurations. The structural optimization of the perfect bulk simulation cell resulted in an MgO lattice parameter a_0 of 4.237 Å. This value is in good agreement with the experimental value of 4.207 Å at 19.8 K.³⁵

The three supercells simulating bulk Mg Frenkel defects relaxed to the same structure: the preferred Mg interstitial site was found to be at the center of a cube of ions. The bulk O Frenkel simulation cell starting with the O interstitial at the center of a cube of ions resulted in a cube-centered interstitial configuration as well. The formation energies for these configurations were found to be 9.0 and 11.0 eV for the bulk Mg and O Frenkel defect, respectively, and compare well with values for cube-centered Frenkel pairs from the literature that, depending on the simulation method, are in the range of 10–14 eV for Mg Frenkel pairs and in the range of 12–15 eV for O Frenkel pairs (see ref 20, and references cited therein).

Whereas most literature studies report formation energies for Frenkel pairs with cube-centered interstitials only, in this study, both from the starting configuration with the O interstitial closer to one of the O lattice atoms (Figure S1b) and from the starting configuration with the O interstitial and one of the O lattice atoms forming a lattice site centered dumbbell (Figure S1c), the O Frenkel interstitial was found to relax into an energetically more favorable $\langle 111 \rangle$ dumbbell configuration, with a defect formation energy of 9.1 eV, the split interstitials being separated by 1.44 Å and each atom having a Bader charge of $-0.85e$. These findings are in excellent agreement with a previous study²⁰ which reported DFT calculations for O^0 and O^- Frenkel defects in MgO besides the usually simulated O^{2-} Frenkel defect. In that study, the O^0 interstitial was shown to relax into a 1.42 Å separated and $-0.8e$ Bader charged $\langle 111 \rangle$ dumbbell configuration and found to be energetically more favorable than the cube-centered interstitial configuration obtained for the O^{2-} Frenkel defect.

A 1996 simulation study³⁶ already found the $\langle 111 \rangle$ oriented and lattice site-centered interstitial dumbbell to be the most stable configuration for the neutral O interstitial in MgO, the constituting atoms being separated by 1.36 Å and each atom having an effective charge of $\approx -1e$. Most recent Frenkel defect studies, however, continued to report results for cube-centered interstitials only (as can be seen, e.g., from the literature overview in the study²⁰ mentioned in the previous paragraph). Studies employing pair potentials are typically limited to systems with fixed and identical charges for same species atoms and are therefore usually unable to find the energetically more favorable dumbbell interstitial. This limitation does not apply when using ab initio methods. Most ab initio Frenkel defect studies, nonetheless, also kept identifying the cube-centered configuration as the most stable configuration, continuing to consider cube-centered input configurations and/or doubly charged defects only, apparently. The study²⁰ already referred to that identified the dumbbell configuration as the most stable configuration for the O^0 Frenkel defect, investigated neutral and singly and doubly charged Frenkel pairs, and did include input configurations other than the cube-centered configuration. In that study, however, after enforcing a particular charge state of the defects, interstitial formation energies were calculated and combined with separately calculated vacancy formation energies to obtain Frenkel defect formation energies. In the present study, the complete Frenkel defect was

simulated within a single supercell, allowing any possible charge state of the point defects as the Frenkel adatom/interstitial and the vacancy can transfer charge to each other, which is a more reliable way of simulating the Frenkel defect.⁹ The cube-centered and dumbbell configurations for the O Frenkel defect in the MgO bulk as obtained after full relaxation are shown in Figure 1.

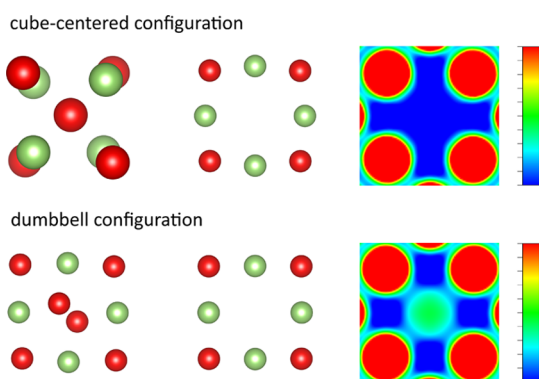


Figure 1. Relaxed cube-centered and dumbbell configurations and vacancy charge density plots for the O Frenkel defect in the MgO bulk. The left and middle panels show the [001] projection of the interstitial and vacancy atomic configurations, including (only) the first shell of surrounding atoms. Light green and red spheres denote Mg and O atoms, respectively. For the middle panel vacancy configurations, the right panels show the charge density (001) cross sections ranging from (blue) 0.07 to (red) 0.27 $e/\text{\AA}^3$.

The defect formation energies calculated for the bulk Schottky pair and dimer are 5.1 and 3.7 eV, respectively. These values are in good agreement with values reported from previous simulations (see refs.^{10,11,20} and references cited therein). A summary of the calculated defect formation energies is given in Table 1.

Surface Defect Configurations. For the Mg Frenkel defect at the MgO{100} surface, no previous calculations were found in the literature. In our study, we identified five different surface Mg Frenkel configurations, as shown in Figure S2a–e and listed in Table 1. Three of these were found to be the lowest energy configurations: the square 1, square 2, and (100) plane dumbbell configurations were all found to have a similar lowest formation energy of 7.2 eV. The square 1 and square 2 configurations are the unpolarized and spin-polarized versions of an otherwise identical structure, respectively, the square 2 configuration containing low levels of spin polarization. The (100) plane dumbbell is a symmetric dumbbell, consisting of two equally Bader charged atoms within the (100) plane. Of higher energy is the top-O configuration. The top-Mg dumbbell configuration was found to be the highest energy Mg Frenkel configuration.

The O Frenkel defect at the MgO{100} surface has been investigated before. In our study, we identified nine different surface O Frenkel configurations, as shown in Figure S2f–n and listed in Table 1. The configurations with the lowest formation energy were found to be the two spin-polarized displaced square configurations displayed in Figure S2f,g. These two lowest energy configurations, with a formation energy of 6.2 eV, have not been reported in the literature before. The configuration that has been reported in the literature as the lowest energy configuration for the surface O Frenkel defect is a spin-polarized top-Mg configuration.⁹ This

top-Mg configuration is among our results as well, where it is referred to as top-Mg 1 (Figure S2i), but we found this configuration to be energetically less favorable than the displaced square configurations, by 0.3 eV. A configuration with a similar formation energy as this top-Mg 1 configuration is the (100) plane dumbbell 1 configuration (Figure S2h), which is an asymmetric dumbbell configuration, the dumbbell consisting of two same species but unequally Bader charged atoms within the (100) plane. Another top-Mg configuration among our results is the top-Mg 2 configuration (Figure S2m). The top-Mg 1 and top-Mg 2 configurations are nearly identical structures, with the O Frenkel adatom located on top of a Mg surface atom at distances of 1.96 and 1.92 \AA , respectively. They greatly differ, however, in magnetism and formation energy: whereas the nonmagnetic top-Mg 2 configuration belongs to our highest energy configurations, the O Frenkel adatom was found to have the largest magnetic moment in the top-Mg 1 configuration, which is among our energetically more favorable configurations. The other highest formation energy configuration is the (100) plane dumbbell 3 configuration (Figure S2n), which is a nonmagnetic configuration as well. The remaining square, (110) plane dumbbell, and (100) plane dumbbell 2 configurations (Figure S2j,k,l) were also found to be nonmagnetic and of higher formation energy than any of the magnetic configurations.

Comparing the Mg and O surface Frenkel defect configurations, it can be observed that spin-polarized configurations are always energetically more favorable than non-spin-polarized configurations for the O Frenkel defect, whereas for the Mg Frenkel defect, spin-polarized solutions are not necessarily preferred over non-spin-polarized solutions. The Mg Frenkel square 1 and square 2 configurations, for example, identical structures differing only in spin-polarization, were found to be equally favorable. The O Frenkel square configuration, on the other hand, was found to be less favorable than its two spin-polarized counterparts. Spin polarization not only lowered the formation energy for the latter: where the Mg Frenkel square defect was found to retain its perfect square character upon spin polarization, for the O Frenkel defect, the magnetic moments on the adatom and in the vacancy led to displacement of the adatom, away from the vacancy and resulting in the O Frenkel displaced square 1 configuration when antiparallel aligned (Figure S2f), and toward the vacancy and resulting in the equally favorable displaced square 2 configuration when parallel aligned (Figure S2g). Here, “parallel aligned” indicates that excess spin-up electron density is located both at the adatom and at the vacancy, while “antiparallel” indicates that excess spin-up electron density is located at the adatom and excess spin-down electron density is located at the vacancy or vice versa.

Comparing the spin-polarized calculations, another notable difference between the Mg and O surface Frenkel defects can be observed: For the O Frenkel defect, the spin-polarized top-Mg and bridge input configurations were found to relax into the spin-polarized top-Mg 1 and (100) plane dumbbell 1 configurations when placing the adatom at an initial distance of $1/2 a_0$ from the surface. When starting with the O Frenkel adatom at a distance of $1/4 a_0$ from the surface, however, these input configurations resulted in the energetically less favorable unpolarized top-Mg 2 and (100) plane dumbbell 2 configurations. Such a dependence on the adatom’s starting height, of the degree of spin polarization and of the consequent

Table 1. Calculated Defect Formation Energy (E_{form}), and Bader Volume Evaluated Electronic Charges (q_{B}) and Magnetic Moments (N) for Frenkel and Schottky Defect Configurations in the MgO Bulk and at the MgO{100} Surface^a

defect configuration	E_{form} (eV)	N_{cell} (μ_{B})	N_{adatom} (μ_{B})	N_{vacancy} (μ_{B}) ^c	$q_{\text{B,Frenkel atom}}$ (e)	$q_{\text{B,1NN}}$ (e)	$q_{\text{B,2NN}}$ (e)	$q_{\text{B,vacancy}}$ (e)	$q_{\text{B,1NN}}$ (e)	$q_{\text{B,2NN}}$ (e)	
Mg Frenkel Bulk											
cube-centered	9.01			+1.53		-1.65 (1.86 Å)	+1.61 (2.33 Å)	0.00	-1.61	+1.65	
square 1 (Figure S2a)	7.19	0.00	0.00	0.00	+1.48 [1.94 Å]	-1.65 (1.90 Å)	+1.62 (2.64 Å)	0.00	-1.60	+1.66	
square 2 (Figure S2b)	7.18	0.39	0.12	0.00	+1.42 [1.94 Å]	-1.65 (1.91 Å)	+1.62 (2.64 Å)	0.00	-1.58	+1.66	
(100) plane dumbbell ^b (Figure S2c)	7.21	0.00	0.00	0.00	+1.59 [1.62 Å]	-1.64 (1.88 Å)	-1.65 (2.05 Å)	0.00	-1.61	+1.66	
top-O (Figure S2d)	7.70	2.36	0.77	0.00	+0.87 [2.37 Å]	-1.71 (1.89 Å)	+1.64 (3.24 Å)	0.00	-1.45	+1.66	
top-Mg dumbbell (Figure S2e)	8.16	0.00	0.00	0.00	+1.59 [1.61 Å]	+1.60 (2.14 Å)	-1.65 (2.25 Å)	0.00	-1.61	+1.66	
O Frenkel Bulk											
cube-centered	10.99			-1.42		+1.65 (1.88 Å)	-1.58 (2.30 Å)	-0.07	+1.61	-1.67	
(111) dumbbell	9.08			-0.85		-0.85 (1.44 Å)	+1.65 (1.94 Å)	-1.17	+1.61	-1.67	
O Frenkel Surface											
displaced square 1 (Figure S2f)	6.24	0.00	-0.83	0.53	-0.98 [1.82 Å]	+1.67 (2.06 Å)	-1.51 (2.32 Å)	-0.41	+1.59	-1.70	
displaced square 2 (Figure S2g)	6.25	2.00	0.83	0.53	-0.98 [1.82 Å]	+1.67 (2.06 Å)	-1.51 (2.32 Å)	-0.41	+1.59	-1.70	
(100) plane dumbbell 1 (Figure S2h)	6.54	1.99	0.87	0.53	-0.95 [1.97 Å]	+1.66 (1.96 Å)	-1.54 (2.36 Å)	-0.40	+1.59	-1.70	
top-Mg 1 (Figure S2i)	6.57	0.00	0.99	-0.54	-0.86 [2.39 Å]	+1.66 (1.96 Å)	-1.64 (3.22 Å)	-0.41	+1.59	-1.70	
square (Figure S2j)	6.79	0.00	0.00	0.00	-1.26 [2.00 Å]	+1.66 (1.99 Å)	-1.61 (2.66 Å)	0.00	+1.59	-1.71	
(110) plane dumbbell (Figure S2k)	6.92	0.00	0.00	0.00	-0.76 [1.19 Å]	-0.98 (1.53 Å)	+1.66 (2.08 Å)	-0.96	+1.55	-1.69	
(100) plane dumbbell 2 (Figure S2l)	7.03	0.00	0.00	0.00	-0.75 [1.24 Å]	-1.00 (1.53 Å)	+1.66 (2.06 Å)	-0.97	+1.56	-1.69	
top-Mg 2 (Figure S2m)	7.28	0.00	0.00	0.00	-1.01 [2.43 Å]	+1.65 (1.92 Å)	-1.64 (3.26 Å)	-0.14	+1.58	-1.71	
(100) plane dumbbell 3 (Figure S2n)	7.30	0.00	0.00	0.00	-1.09 [1.80 Å]	+1.66 (1.96 Å)	-1.48 (2.25 Å)	-0.23	+1.57	-1.70	
Schottky Bulk											
pair	5.13							0.00	-1.61; +1.63	+1.65; -1.65	
dimer	3.72							0.00	-1.60; +1.63	+1.65; -1.66	
Schottky Surface											
pair (Figure S2o)	4.44							0.00	-1.60; +1.62	+1.66; -1.66	
dimer (Figure S2p)	3.19							0.00	-1.62; +1.63	+1.66; -1.67	

^aBader charges are listed for Frenkel interstitials and adatoms ($q_{\text{B,Frenkel atom}}$) and Frenkel and Schottky vacancies ($q_{\text{B,vacancy}}$), and for the (surface) atoms nearest neighboring ($q_{\text{B,1NN}}$) and second nearest neighboring ($q_{\text{B,2NN}}$) these atoms and sites. The distance of a neighboring atom to a Frenkel interstitial or adatom is given inside parentheses. The distance of a Frenkel adatom perpendicular to the surface is given inside brackets. For Frenkel surface defect configurations, the table includes the net magnetization of the entire defect simulation cell (N_{cell}), and the magnetic moments on the Frenkel adatom (N_{adatom}) and inside the vacancy (N_{vacancy}). ^bIn the Mg Frenkel (100) plane dumbbell configuration, the adatom forms a dumbbell with its third nearest neighboring surface atom. This surface atom is located at a distance of 2.35 Å from the adatom and has a Bader charge of +1.59e: $q_{\text{B,3NN}} = +1.59e$ (2.35 Å). ^cA manual check of the assignment of magnetic moment revealed a misassignment of 0.22 μ_{B} contained within the O vacancies to the five nearest neighboring surface and subsurface Mg atoms for the spin-polarized O Frenkel surface configurations, and these values have been corrected accordingly.

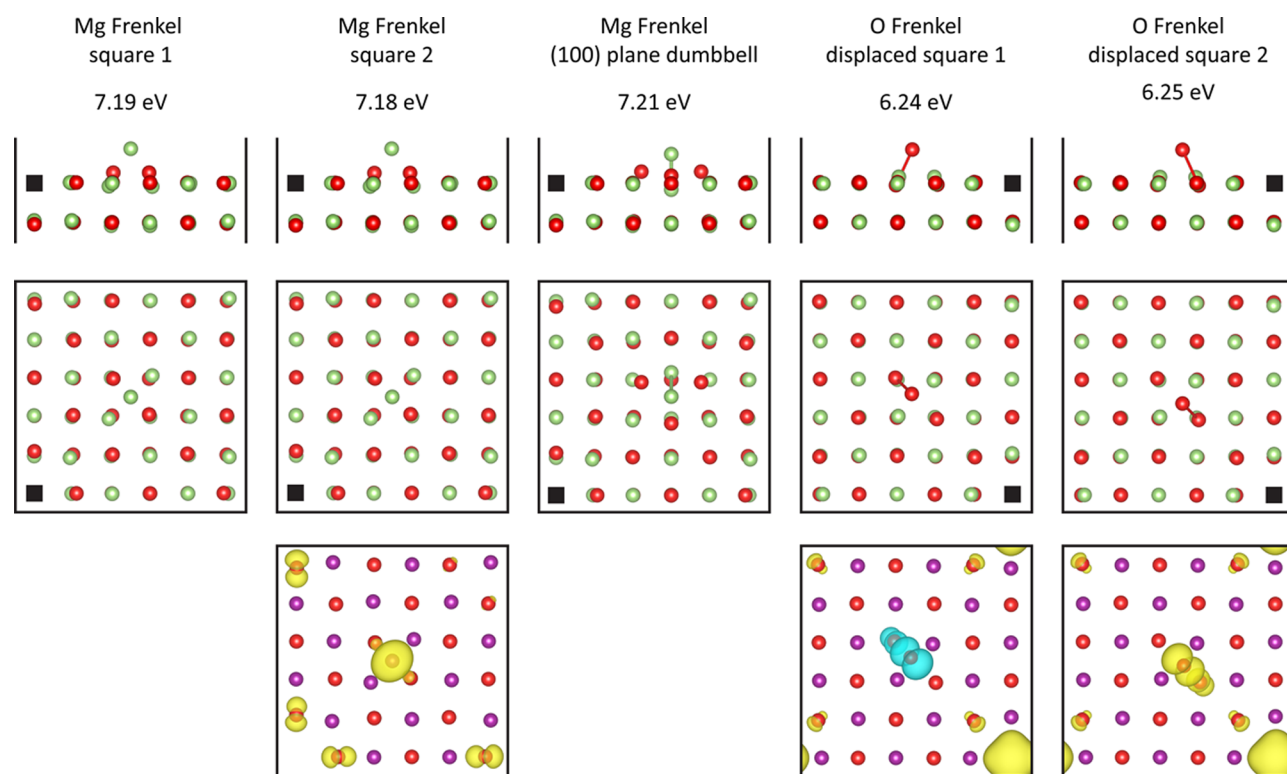


Figure 2. Atomic output configurations and spin-polarization density plots for the energetically most favorable Mg Frenkel and O Frenkel surface defects. The atomic structural models show the [010] and [001] projections of the two top layers of the supercells simulating these defects, as obtained after full relaxation. Light green and red spheres denote Mg and O atoms, respectively. Black squares indicate vacancy sites. Simulation cell boundaries are indicated with a solid line. For the three spin-polarized configurations, spin-polarization density plots are included, showing $0.007 \text{ e}/\text{\AA}^3$ spin-up minus spin-down electron density isosurfaces for the top layer of the spin-polarized Mg Frenkel configuration and $0.019 \text{ e}/\text{\AA}^3$ spin-up minus spin-down electron density isosurfaces for the top layer of the spin-polarized O Frenkel configurations. In these plots, purple and red spheres denote Mg and O atoms, respectively. Net spin-up and net spin-down charge densities are plotted in yellow and blue, respectively. The calculated defect formation energies are included. Atomic output configurations and spin-polarization density plots for all 16 surface defect configurations identified in this study can be found in Figure S2 of the Supporting Information.

relaxation output configuration, was not observed for any of the Mg Frenkel defect configurations.

For Schottky defects at the $\text{MgO}\{100\}$ surface, two simulation studies were found reporting formation energies.^{10,11} The defect formation energies of 4.4 and 3.2 eV calculated here for the surface Schottky pair and surface Schottky dimer, respectively, are in good agreement with those previous investigations.

The lowest energy surface Frenkel configurations are shown in Figure 2, and the lowest energy surface Schottky configurations are shown in Figure 3. As can be seen from Table 1, the surface Schottky defects have 13–14% lower formation energies than the bulk Schottky defects. The formation energies of the lowest energy surface Frenkel defects are even 20–31% lower than the formation energies of their bulk counterparts. The formation energy of 3.2 eV for the surface Schottky dimer is the lowest defect formation energy calculated in this study. This means that all defect configurations we identified have a low probability of being formed thermally at room temperature. Our findings show, however, that when conditions are such that Frenkel and Schottky defects can be formed, Frenkel and Schottky defects are much more likely to be formed at the $\text{MgO}\{100\}$ surface than in the MgO bulk, and that Schottky defects are more favorable than Frenkel defects.

Surface Restructuring. Experimental studies have shown the $\text{MgO}\{100\}$ surface to exhibit inward relaxation and

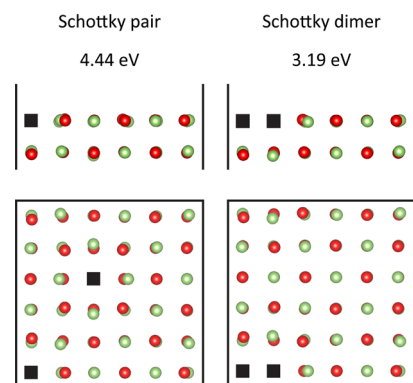


Figure 3. Atomic output configurations for the Schottky surface pair and dimer, as obtained after full relaxation. Top panels show the [010] projection and bottom panels show the [001] projection. Light green and red spheres denote Mg and O atoms, respectively. Black squares indicate vacancy sites. Simulation cell boundaries are indicated with a solid line. The calculated defect formation energies are included.

rumpling: the $\text{MgO}\{100\}$ atomic surface plane has been found to move as a whole toward the bulk, the Mg surface ions displacing toward the bulk more, however, than the O surface ions do (see ref 37, and references cited therein). From our perfect surface simulation cell, no inward relaxation was observed, but the simulated surface was found to rumple: from

the ideal surface plane positions, the Mg ions displaced 0.02 Å toward the bulk and the O ions 0.03 Å away from the bulk. These results compare favorably with results from previous simulations (see refs.^{38,40} and references cited therein).

Mild restructuring was found for the surface atoms neighboring the Schottky pair and Frenkel monovacancies and Schottky dimer divacancies: In the lateral XY direction, nearest neighboring atoms moved away from the vacancy by 0.11–0.27 Å, and the second nearest neighboring atoms moved toward the vacancy by 0.11–0.25 Å. In the direction perpendicular to the surface and relative to the corresponding (rumpled) perfect surface atom sites, the nearest and second nearest atoms showed outward relaxation ranging from –0.04 to +0.09 Å. The resulting displacements agree well with previous calculations for surface Schottky dimers.¹⁰

Frenkel adatoms, relaxing to positions at distances of 1.19–2.43 Å perpendicular to the surface and relative to the corresponding (rumpled) perfect surface atom sites (see Table 1), were found to induce a much stronger restructuring of surface atoms, as can be found illustrated for the lowest energy Frenkel defect configurations in Figure 2 (see also Figure S2).

For the Mg square (Figure S2a,b) and O displaced square (Figure S2f,g) lowest energy configurations, the surface atoms closest to the adatom, of opposite charge and occupying positions at distances of 1.90–2.06 Å to the adatom, showed movement perpendicular to the surface with an outward relaxation of 0.36–0.55 Å and an inward movement of 0.07–0.09 Å in the XY direction. The two closest same species surface atoms, having moved outwardly in the XY direction by 0.10–0.18 Å and occupying positions at distances of 2.32–2.64 Å to the Frenkel adatom, were found to displace inwardly in the Z direction, moving toward the bulk by 0.09–0.13 Å.

The Mg(100) plane dumbbell lowest energy Frenkel configuration (Figure S2c) showed the strongest restructuring of surface atoms. The adatom, forming a 2.35 Å separated dumbbell with the closest Mg surface atom, was found to push away the latter in the Z direction inwardly by 0.32 Å and in the Y direction by 0.39 Å. The closest O surface atom, occupying a position at a distance of 1.88 Å to the adatom, showed an outward relaxation of 0.40 Å in the Z direction and a movement away from the Mg dumbbell of 0.32 Å in the Y direction. The second closest O surface atoms relaxed to positions at a distance of 2.05 Å to the adatom, moving outwardly by 0.62 Å in the Z direction and displacing toward the Mg dumbbell by 0.49 Å in the XY direction. The second closest Mg surface atoms moved to positions at a distance of 2.93 Å to the adatom, relaxing outwardly by 0.05 and 0.15 Å in the Z direction and XY direction, respectively.

The observed relaxations are easily understood from electrostatic principles. The removal of charged atoms results in movement away from a vacancy for the (oppositely charged) nearest neighboring surface atoms and in movement toward a vacancy for the second nearest neighboring surface atoms (having the same type of charge). Likewise depending on the type of charge, the proximity of a charged (Frenkel) atom results in displacements of neighboring atoms away from and toward this atom.

Bader Analysis. To study the distribution of electronic charge in the Schottky and Frenkel defective configurations and the distribution of magnetic moments in the Frenkel defective surface configurations, a Bader charge analysis was carried out. Bader defines the boundary of an atom as the surface where the normal component of the gradient of the

electron density is zero.²⁸ A vacancy trapping electronic charge will have such a demarcating zero-flux surface as well. The charge contained within the volume enclosed by this surface is interpreted as the electronic charge of the atom or the electronic charge trapped by the vacancy. Magnetic moments can be obtained from the Bader charge analysis as well, by evaluating the spin-up and spin-down electron densities within Bader volumes.

Bader Analysis Bulk Defects. For the MgO bulk defect configurations, a summary of the Bader-calculated electronic charges for defect sites and the nearest and second nearest neighboring atoms can be found in Table 1.

Bader charges of $\pm 1.65e$ were calculated for defect-free MgO bulk atoms. For the cube-centered Mg and O interstitial atoms, the Bader charge analysis resulted in charges of +1.53e and –1.42e, respectively. As can be seen from Table 1, the Bader charges for the nearest (opposite species) neighbors of Frenkel interstitial atoms remain an unaffected $\pm 1.65e$ perfect bulk value; the second nearest neighboring (same species) atoms are slightly less charged than perfect bulk atoms. The calculated values compare well with results found in the literature for perfect bulk atoms and cube-centered interstitials.^{16,20,41,42} The O atoms forming the energetically more favorable $\langle 111 \rangle$ dumbbell interstitial configurations were found to be –0.85e Bader charged each, in excellent agreement with a previous study,²⁰ as mentioned before.

The atoms neighboring bulk vacancy sites show Bader charges that vary with the $\pm 1.65e$ perfect bulk value by only a few 0.01e. As for the vacancies themselves, most interestingly, as can be seen from Figure 1, and in contrast to the other Frenkel and Schottky vacancies, a significant amount of charge was found to be trapped by the O vacancy that is a part of the lowest energy O Frenkel pair (with the $\langle 111 \rangle$ dumbbell interstitial). Bader charge analysis revealed this trapped charge to amount to –1.17e. The trapped charge affects the relaxation of neighboring atoms: compared to the cube-centered interstitial O Frenkel configuration (see Figure 1), the Mg atoms nearest neighboring the O Frenkel vacancy that is a part of the $\langle 111 \rangle$ dumbbell interstitial configuration showed a decreased outward relaxation, by 0.17 Å, while the second nearest neighboring (O) atoms' inward relaxation decreased by 0.07 Å.

Bader Analysis Surface Defects. For atoms belonging to the defect-free MgO{100} surface, the Bader charges were found to equal the perfect bulk value of $\pm 1.65e$, in agreement with previous simulations for perfect MgO surface atoms.^{16,43} The lowest energy surface Frenkel configurations were found to result in Bader charges ranging from +1.42e to +1.59e for Mg adatoms and in Bader charges of –0.98e for O adatoms. In general, the transfer of negative charges (electrons) away from the adatom increases with decreasing distance to the surface (see Table 1). The increased transfer of electrons away from the adatom causes the Bader charge for O adatoms to decrease from –1.3e to –0.8e when going from a perpendicular distance of 2.0 Å to distances of 1.2 Å. A similar but smaller effect was observed for Mg adatoms, for which the increased transfer of negative charge away from the adatom was found to result in an increase in the Bader charge, from +1.4e to +1.5e, respectively, to +1.6e when going from distances of 1.9 Å to distances of 1.6 Å. Exceptions are the O Frenkel top-Mg configurations (Figure S2i,m) and the Mg Frenkel top-O configuration (Figure S2d), for which the adatoms, while located at distances normal to the surface of 2.4 Å, were found

to have Bader charges of $-0.9e$, $-1.0e$, and $+0.9e$, respectively. The adatoms in these configurations have smaller Bader charges than what would be expected based on the trends observed for the adatoms in the other Frenkel configurations.

From Table 1, it can be seen that surface atoms neighboring a same species Frenkel adatom have Bader charges that show only little deviation from the perfect surface value for Mg atoms, but have much larger deviations that decrease with increasing distance to the adatom for O atoms. When co-constituting a surface dumbbell, surface atoms were found to have a smaller electronic charge than when neighboring a same species adatom in perfect square or top (not: top-dumbbell) configurations. For the Mg Frenkel surface dumbbells (Figure S2c,e), the Bader analysis resulted in equal Bader charges of $+1.6e$ for each of the constituting Mg atoms. The O Frenkel surface dumbbells (Figure S2h,k,l,n) were all found to be asymmetric, the adatom either having a Bader charge of $-0.8e$ and forming a 1.5 \AA separated dumbbell with its $-1.0e$ Bader-charged nearest neighbor, or having a Bader charge of $-1.0e$ and forming a 2.3 \AA separated dumbbell with its $-1.5e$ Bader-charged second nearest neighbor. The values obtained for the latter were found to be equal to those for the lowest energy displaced square O Frenkel configurations (that are in fact also asymmetric dumbbells; Figure S2f,g). For the surface atoms neighboring Frenkel adatoms of the opposite species, Bader charges were calculated, that just like their bulk counterparts showed no (to little) deviation from the perfect value.

Atoms neighboring surface vacancies were found to have Bader charges that vary only slightly from the perfect surface values by up to a few $0.01e$. An exception is the Mg Frenkel top-O configuration (Figure S2d), for which the O atoms nearest neighboring the Mg vacancy were found to be less Bader-charged than the perfect O surface atoms by $0.2e$. The Mg adatom in this configuration, at the same time, was found to have an atypically smaller Bader charge of $+0.9e$, the Bader charge for the Mg adatoms in the other Mg surface Frenkel configurations ranging from $+1.4e$ to $+1.6e$. It appears that in the Mg Frenkel top-O configuration, which is a higher-energy Mg surface Frenkel configuration with the adatom at a distance of 2.4 \AA from the surface, transfer of electronic charge from the adatom region of the surface toward the vacancy region of the surface is partially inhibited. This seems to be evidenced by the larger Bader charge calculated for the O atoms that are nearest neighboring the Mg adatom, with these atoms accepting more electronic charge than the nearest neighboring O atoms in the other Mg surface Frenkel configurations do.

In contrast to the Mg Frenkel top-O configuration discussed in the previous paragraph, the Mg vacancy regions in the remaining Mg Frenkel configurations were all found to be only slightly charged. For the Schottky Mg and O vacancy regions, as can be seen from the net Bader charge of these vacancies' nearest and second nearest neighboring surface atoms, Bader analysis resulted in only small net Bader charges as well. For the O Frenkel configurations, however, the electronic charge contained within the O vacancy region was found to be significantly larger due to the trapping of significant amounts of charge inside the vacancies. Such trapping of charge was not observed for the Mg Frenkel and Schottky configurations. (The O Frenkel square configuration vacancy was also not found to trap any charge. This square configuration is the only exception among the O Frenkel configurations in this regard and may be considered the surface analogue of the bulk cube-centered O Frenkel configuration.) The amount of trapped

charge is the largest ($-1.0e$) for the vacancies that are a part of configurations in which the O adatoms form dumbbells with the nearest neighboring surface atoms. As we saw before, these dumbbells show smaller Bader charges than the adatoms and dumbbell co-constituting surface atoms in other configurations do. Apparently, this lower amount of electronic charge on the dumbbells is accommodated by an increased transfer of electronic charge into the vacancies. The lowest energy O Frenkel configurations were found to trap $-0.4e$ inside the vacancy.

Table 1 includes magnetic moments calculated for the surface Frenkel configurations. The corresponding spin-polarization densities can be found in Figure S2. As can be seen from Table 1, for the two spin-polarized Mg Frenkel configurations, Mg adatoms were found to have magnetic moments varying from $0.8 \mu_B$ for the Mg top-O configuration (shown in Figure S2d) to $0.1 \mu_B$ for the Mg square 2 configuration (shown in Figure S2b). These amounts account for about one-third of the total amount of magnetic moments contained within the simulation cells for these defects: the atomic magnetic moments in these cells are parallel aligned and add up to a net magnetization of the respective simulation cells of 2.4 and $0.4 \mu_B$. The remaining two-third was found to originate from O atoms, the four O surface atoms nearest neighboring the vacancy sites, with summed magnetic moments of 0.9 and $0.2 \mu_B$ for the Mg top-O and Mg square 2 configuration, respectively, contributing the most.

For the spin-polarized O Frenkel configurations, Bader analysis revealed the O adatoms to have magnetic moments with magnitudes ranging from 0.8 to $1.0 \mu_B$. The O displaced square 2 and (100) plane dumbbell 1 simulation cells (Figure S2g,h) were found to contain a total amount of $2.0 \mu_B$ parallel aligned atomic magnetic moments. For the O displaced square 1 and top-Mg 1 defect simulation cells (Figure S2f,i), a zero net magnetization of $0.0 \mu_B$ was observed, while these cells contain equal total amounts ($1.0 \mu_B$) of antiparallel oriented atomic magnetic moments. In each of the O Frenkel simulation cells, the adatom region was observed to contain a total amount of $1.0 \mu_B$ similarly oriented atomic magnetic moments, the net amount of the magnetic moment originating from the O adatom and its nearest neighboring surface O atom (for the O top-Mg 1 configuration, Figure S2i: its two nearest neighboring surface O atoms), always fully adding up to this $1.0 \mu_B$. The remaining $1.0 \mu_B$ contained within the simulation cells, parallel aligned to the magnetic moments contained within the adatom region for the O displaced square 2 and (100) plane dumbbell 1 configurations (Figure S2g,h) and antiparallel for the O displaced square 1 and top-Mg 1 configurations (Figure S2f,i), was found to be located for the most part at the vacancy sites ($0.5 \mu_B$) and the vacancies' nearest neighboring surface and subsurface O atoms (contributing 0.3 and $0.1 \mu_B$, respectively). Here, "parallel aligned" indicates that excess spin-up electron density is located both at the adatom and at the vacancy, while "antiparallel" indicates that excess spin-up electron density is located at the adatom and excess spin-down electron density is located at the vacancy or vice versa.

It is the antiparallel versus parallel alignment of the adatom and vacancy regions' magnetic moments that causes the O Frenkel displaced square 1 and 2 configurations to be structurally different. As can be seen from Table 1, these configurations are very similar in terms of Bader charges and interatomic distances and have identical Bader charges at the

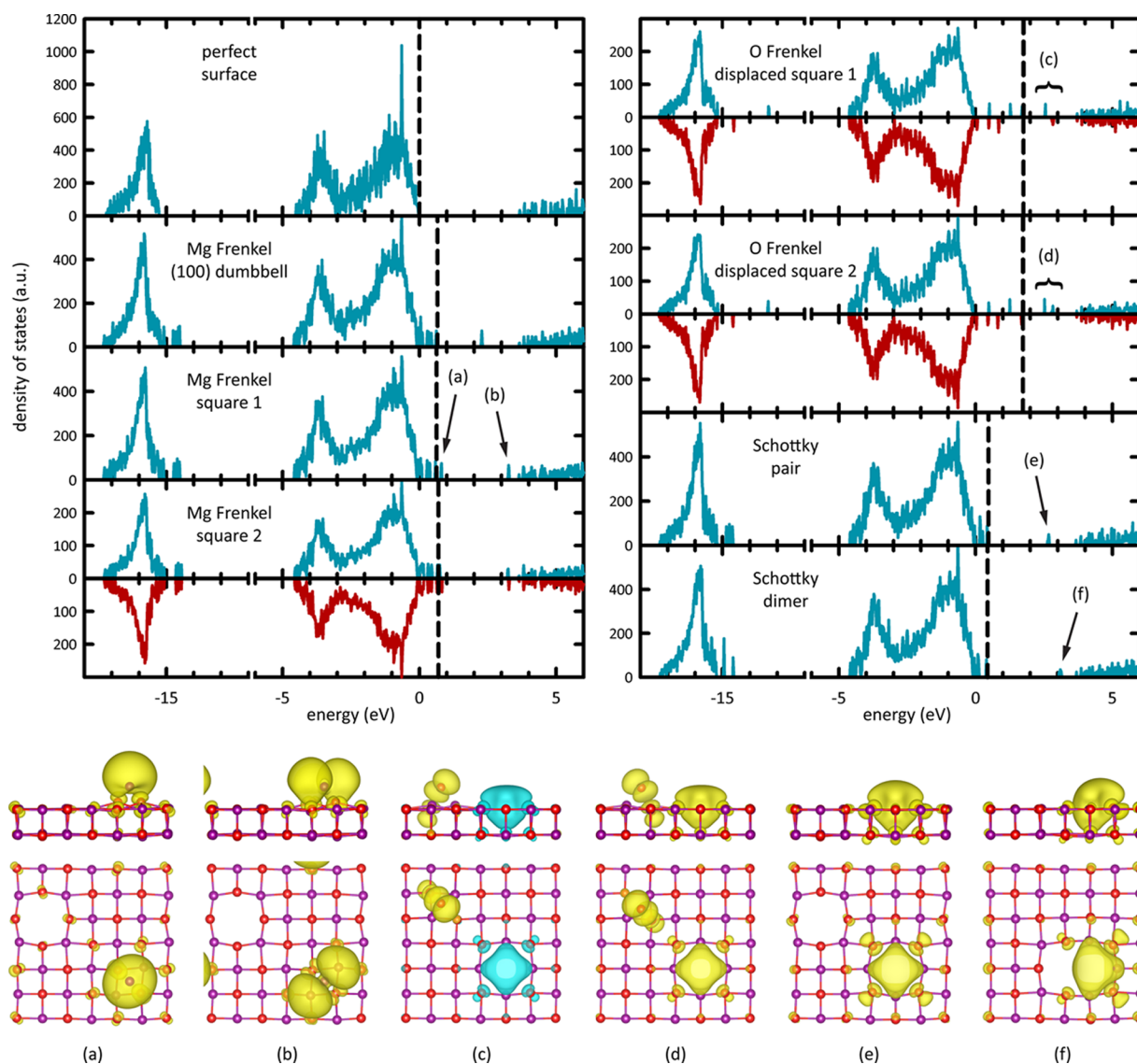


Figure 4. Top panels: DOS plots for the perfect MgO{100} surface and the lowest energy Frenkel and Schottky defect configurations. Fermi levels are indicated with dashed black lines. The plots are aligned with respect to their highest O 2p peaks while the Fermi level of the perfect surface is set to zero, so that all energies are relative to the VBM of the perfect surface. For spin-polarized configurations, spin-up and spin-down states are plotted in blue and red, respectively. For unpolarized configurations, the plot shows the total DOS (in blue). Bottom panels, (a–f): side and top views of the band decomposed charge densities for the peaks labeled (a–f) in the upper panel DOS plots. The side projections show two atomic layers, purple and red spheres denoting Mg and O atoms, respectively. The top projections show only the defective surface layer (which includes the adatom for Frenkel defective layers). All charge density plots show $0.007 \text{ e}/\text{\AA}^3$ isosurfaces. For the unpolarized configurations, in (a,b) and (e,f), the total charge density is plotted (in yellow). For the spin-polarized configurations, in (c,d), the majority and minority spin charge densities (that were found to have no spatial overlap) are plotted in yellow and blue, respectively.

adatoms and inside the vacancies. That the adatom nonetheless displaces away from the vacancy in the displaced square 1 configuration but toward the vacancy in the displaced square 2 configuration is the result of their magnetic moments being antiparallel and parallel aligned, respectively.

The charge effects observed for the Frenkel and Schottky defective surfaces, in particular, the decreased ionicity of adatoms and surface atoms, the trapping of electronic charge inside vacancies, and the transfer of electronic charge between adatom and vacancy regions, are a strong indication of chemical activation of the MgO{100} surface. Decreased ionicity and trapped charge cause atoms and vacancies to accept and donate electronic charge more easily, which allows a more readily binding or dissociation of molecules and ions at

the MgO{100} surface. Transfer of charge within layers may be a part of the mechanism that sustains a chemical reaction.

Density of States. To investigate how the Schottky and Frenkel defects affect the electronic structure of the MgO{100} surface, we analyzed the DOS of these defects. Figure 4 shows the DOS for the perfect MgO surface and for the energetically most favorable Frenkel and Schottky defective surfaces. To allow easier comparison and discussion, the plots are aligned with respect to the highest O 2p peak. Fermi levels are indicated with a dashed line and is set to zero only for the perfect surface. Consequently, all energies in Figure 4 are relative to the valence band maximum (VBM) of the perfect surface, and the Fermi levels of the defective surface configurations that have shifted to mid-band gap positions

that depend on the electronic occupation of defect states are located in Figure 4 at positive values.

In the DOS plots of Figure 4, we have indicated several interesting mid-band gap defect states with arrows and brackets and labeled these (a–f). At the bottom of Figure 4, the corresponding panels (a–f) show the partial charge densities (total, spin-up, or spin-down electron densities) belonging to these unoccupied defect states. These partial charge densities were generated from the total charge density by setting energy windows over the respective peaks in the DOS using standard VASP software options. Figure S3 also shows, in addition to the total DOS, the projected DOS (pDOS) of the Mg and O adatoms for the three Mg Frenkel and two O Frenkel defect configurations and which peaks in the total DOS are associated with the Frenkel vacancies.

The DOS of the perfect surface was found to display a narrow band of O 2s states at energies between -17.2 and -15.2 eV and a broader two-peak O 2p band which forms the valence band between -4.6 and 0.0 eV. A band gap of 3.6 eV separates the top of the valence band and the bottom of the conduction band, which consists of unoccupied Mg 3s states. The shape, width, and position of the DOS peaks, and the value of the band gap, compare well with results from previous simulation studies (see refs. ^{8,39,40,44,45} and references cited therein). Experimental studies have found the surface band gap of MgO{100} to be larger than our DFT-calculated value of 3.6 eV, namely, 6.2 eV.^{46,47} Underestimation of the band gap is a common feature of DFT calculations. We expect our DFT-calculated results on the mid-band gap defect states to be scalable with respect to the experimental values.

As can be seen from Figure 4, the Schottky, Mg Frenkel, and O Frenkel defects all result in occupied defect states above the top of the valence band, elevating the Fermi level by 0.4 – 0.5 , 0.6 – 0.7 , and 1.7 eV, respectively. Unoccupied mid-band gap states between the valence and conduction band and the introduction of states between the O 2s and O 2p peak can be clearly observed for all defects as well.

O vacancies at the MgO{100} surface are known to result in a mid-gap defect state between the top of the valence band and the bottom of the conduction band of the perfect MgO{100} surface.^{8,13,39} In our study, for the Schottky pair and Schottky dimer defect configurations, a mid-gap peak was found at energies, relative to the elevated Fermi level, of 2.2 and 2.7 eV, respectively (in Figure 4, relative to the VBM of the perfect surface: at 2.7 and 3.1 eV, respectively). Analysis showed this mid-gap peak to mainly consist of O vacancy states, and to a lesser extent, of states that are associated with the O vacancy's neighboring O atoms and that are predominantly O 2p in nature, as can be found illustrated in Figure 4e,f. O atoms neighboring the Mg vacancy were found to be the origin of the split off (occupied O 2p) states at the top of the valence band and of the (O 2s) states split off from the O 2s peak as well.

The Mg vacancies in the Mg Frenkel defect configurations introduce defect states to the DOS of the perfect MgO surface in a similar way the Mg vacancies in the Schottky defect configurations do: through their presence, the Mg vacancies result in the observed splitting off of (occupied) O 2p and O 2s states that are associated with (neighboring) O atoms. For the Mg(100) dumbbell configuration, the formation of one mid-gap peak at an energy of 1.6 eV above the Fermi level was seen, whereas for the Mg square 1 configuration, two peaks of unoccupied defect states inside the band gap were found, one above the top of the valence band at an energy of 0.2 eV and

one below the conduction band at an energy of 2.6 eV above the Fermi level. In Figure 4, at the energy scale relative to the VBM of the perfect surface, these peaks are located at energies of 2.3 , 0.8 , and 3.2 eV. (DOS analysis results for the Mg square 2 configuration were found to be very similar to the Mg square 1 configuration DOS analysis results and will not be discussed here separately.) Analysis showed the unoccupied defect states to be mainly localized on the Mg adatom (see for the pDOS of the Mg adatoms Figure S3a–c), and, to a lesser extent, on the Mg adatom's neighboring O atoms. The states associated with the latter are of a predominantly O 2p nature. The states associated with the Mg adatom in the mid-gap peak of the Mg(100) dumbbell configuration and the states associated with the Mg adatom in the peak above the valence band of the Mg square 1 configuration were found to have both Mg 3s and Mg 3p characteristics. In contrast, and as can be found illustrated in Figure 4a,b, the states associated with the Mg adatom in the peak below the conduction band of the Mg square 1 configuration were found to have mainly Mg 3p features. The Mg adatom defect states vastly extend into the vacuum, as can be seen from Figure 4a,b as well.

Whereas the O vacancies in the Schottky defect configurations were found to introduce one peak of unoccupied defect states in the band gap of the perfect MgO{100} surface, the O vacancies in the lowest energy O Frenkel defective configurations were found to introduce two peaks of defect states: one peak of unoccupied states at an energy of 1.1 eV above the elevated Fermi level (i.e., the right peak of the two unoccupied mid-gap peaks) and one peak of occupied states at an energy of -0.05 eV right below the elevated Fermi level. In Figure 4, at the energy scale that is set to zero for the Fermi energy of the perfect surface, these peaks are located at 2.8 and 1.7 eV, respectively; in Figure S3d,e, these defect states are indicated with arrows. The O atoms neighboring the vacancies were found to contribute (O 2p) states to these peaks as well, as can be found illustrated for the unoccupied defect states peaks in Figure 4c,d. As can be seen from the DOS plots in Figure 4, and from the more detailed DOS plots in Figure S3d,e as well, the occupied and unoccupied vacancy defect states are always of opposite spin species. For the displaced square 1 configuration, for example, the occupied vacancy defect state peak was found to contain majority spin states only, whereas the corresponding unoccupied defect state peak solely consists of minority spin states. The remainder of the occupied defect states introduced at the top of the valence band in the displaced square 1 and 2 configurations were found to have O 2p characteristics and to be associated with the adatom and the two O surface atoms nearest and second nearest neighboring the adatom. These atoms, with a major contribution from the O adatom, were also observed to be the origin of the (O 2s) defect states introduced at the energies of -16.3 and -15.0 eV below the elevated Fermi level, as is also clear from the pDOS plots shown in Figure S3d,e.

The unoccupied defect states in the (left) mid-gap peak observed in the DOS for the displaced square 1 and 2 configurations at an energy of 0.8 eV above the elevated Fermi level were found to belong to O 2p orbitals that are associated with the adatom and the O surface atom nearest neighboring the adatom. (At the energy scale used in Figure 4, these peaks are located at 2.5 eV.). As can be seen from the DOS plots and the partial charge densities shown in Figure 4c,d, and from Figure S3d,e as well, the (left) mid-gap peak states associated with the displaced square 1 and 2 adatoms are always majority

spin states. The (right) mid-gap peak states originating from the corresponding vacancies were found to be either solely minority spin states, in the displaced square 1 configuration, or solely majority spin states, in the displaced square 2 configuration. Note that this is in contrast to the study⁹ mentioned earlier and identifying a top-Mg configuration as the lowest energy configuration for the O surface Frenkel defect, in which the two mid-gap peaks in the DOS for that configuration were found to solely consist of minority spin states.

For the effect on the surface chemistry of the perfect MgO{100} surface, the defect states introduced in the band gap of the latter are the most relevant, in particular, those that are unoccupied by electrons in the ground state. Unoccupied defect states (acceptor states) may more easily accept electrons excited from the MgO valence band or donated by the involved non-MgO reactant and consequently facilitate the role that these electrons play in chemical reactions. Occupied defect states (donor states) may facilitate the more readily excitation of electrons from the MgO valence band. For the Mg Frenkel and Schottky defects, the states introduced in the perfect surface band gap that are occupied were found to result in a prolongation of the perfect surface valence band by less than 1 eV. The occupied states introduced by the O Frenkel defects, on the other hand, are well isolated and sharp, indicating a strongly localized nature of these defect states, and were found to shift the Fermi level more considerably, by nearly 2 eV. The unoccupied defect state peaks introduced by the O Frenkel defects were, furthermore, observed to be larger in number (two instead of one) and closer to the Fermi level than the unoccupied defect state peaks in the Schottky and Mg Frenkel (100) dumbbell defect configurations. The Mg Frenkel square defects were found to result in two unoccupied defect state peaks as well. These two peaks, however, are very closely located to the top of the valence band and the bottom of the conduction band. A peak that is that close to the top of the valence band may very well act as the top of a valence band, whereas a peak that is that close to the bottom of the conduction band may still not very easily accept electrons and perhaps even act as the bottom of the conduction band, in which case the two peaks may be considered as effectively constituting a less wide but still defect state-free band gap. Considering all this, all Schottky and O Frenkel and Mg dumbbell Frenkel defects (but perhaps the Mg square Frenkel defects as well) can be expected to play a role in the chemical activation of MgO. The O Frenkel defects, in particular, can be expected to greatly enhance the reactivity of the MgO{100} surface.

CONCLUSIONS

We have presented the results from our DFT study of Schottky and Frenkel defects at the MgO{100} surface performed in light of the chemical activation of MgO. We identified three lowest energy surface Mg Frenkel defects. These were found to include (one) dumbbell-type reconstructed and (two) square-centered adatom configurations, with low levels of spin polarization for only one of the latter two. The two lowest energy surface O Frenkel defects are both spin-polarized. The magnetic moments on the adatom and inside the vacancy in these defect configurations were found to cause the adatom to move away from the vacancy when antiparallel aligned and toward the vacancy when parallel aligned and to result in two

structurally different (displaced square) dumbbell-type reconstructed adatom configurations.

Calculation of bulk and surface defect formation energies shows that Frenkel and Schottky defects are more likely to be formed at the surface than in the bulk. In the surface Frenkel defect configurations, adatoms were found to induce a strong local restructuring of surface atoms. Bader charge analysis revealed a largely decreased ionicity for the adatoms, and for the surface atoms co-constituting dumbbells as well. A transfer of electronic charge was found to take place between the adatom and vacancy regions in Frenkel defect configurations. The two effects are strongest for O Frenkel defects. O Frenkel vacancies were also observed to trap significant amounts of electronic charge; in contrast to the Mg and O vacancies in the Mg Frenkel and Schottky defect configurations, which were not found to trap any charge. Investigation of the DOS of the Frenkel and Schottky defective surfaces shows that all considered defects introduce many electronic defect states in the wide band gap of perfect MgO. Analysis revealed these states to be associated with the O vacancies and Mg and O adatoms, and suggests that, in particular, the O Frenkel defects can be expected to greatly enhance the reactivity of the MgO surface.

Our findings are a strong indication that the defective MgO surface is chemically not inert and will more readily bind or dissociate molecules and ions. A full exploration of the effects of Frenkel and Schottky defects on the surface chemistry of MgO requires explicit simulation of the adsorption of specific molecular and ionic species at Schottky and Frenkel adatom and vacancy defect sites. The present study has identified the surface defects that are most likely to be involved in chemical reactions, and these can be used as a starting point in future simulation studies of defect-induced surface reactivity of MgO.

ASSOCIATED CONTENT

Supporting Information

The Supporting Information is available free of charge on the ACS Publications website at DOI: 10.1021/acs.jpcc.9b01908.

Input configurations for Frenkel interstitials and adatoms, output configurations and spin-polarization density plots of all surface Frenkel defects and surface Schottky defects, additional DOS plots of Frenkel surface defects (PDF)

AUTHOR INFORMATION

Corresponding Author

*E-mail: h.vangog@uu.nl

ORCID

Marijn A. van Huis: 0000-0002-8039-2256

Author Contributions

HvG conceived the study, performed the calculations, and wrote the manuscript. MAVH commented on the manuscript.

Notes

The authors declare no competing financial interest.

ACKNOWLEDGMENTS

This work was carried out on the Dutch national e-infrastructure with the support of SURF Cooperative. Figures of atomic structural models and charge densities were produced using VESTA.⁴⁸

REFERENCES

- (1) Stirniman, M. J.; Huang, C.; Scott Smith, R.; Joyce, S. A.; Kay, B. D. The adsorption and desorption of water on single crystal MgO(100): The role of surface defects. *J. Chem. Phys.* **1996**, *105*, 1295–1298.
- (2) Newberg, J. T.; Starr, D. E.; Yamamoto, S.; Kaya, S.; Kendelewicz, T.; Mysak, E. R.; Porsgaard, S.; Porsgaard, S.; Salmeron, M. B., Jr.; Brown, G. E.; et al. Autocatalytic surface hydroxylation of MgO(100) terrace sites observed under ambient conditions. *J. Phys. Chem. C* **2011**, *115*, 12864–12872.
- (3) Sasahara, A.; Murakami, T.; Tomitori, M. Hydration of MgO(100) surface promoted at <011> steps. *J. Phys. Chem. C* **2015**, *119*, 8250–8257.
- (4) Liu, P.; Kendelewicz, T.; Brown, G. E., Jr. Reaction of water with MgO(100) surfaces. Part II: Synchrotron photoemission studies of defective surfaces. *Surf. Sci.* **1998**, *412-413*, 315–332.
- (5) Gajdardziska-Josifovska, M.; Sharma, R. Interaction of oxide surfaces with water: Environmental transmission electron microscopy of MgO hydroxylation. *Microsc. Microanal.* **2005**, *11*, 524–533.
- (6) Lu, Y.; Geng, J.; Wang, K.; Zhang, W.; Ding, W.; Zhang, Z.; Xie, S.; Dai, H.; Chen, F.-R.; Sui, M. Modifying surface chemistry of metal oxides for boosting dissolution kinetics in water by liquid cell electron microscopy. *ACS Nano* **2017**, *11*, 8018–8025.
- (7) Shen, Y.; Xu, T.; Tan, X.; Sun, J.; He, L.; Yin, K.; Zhou, Y.; Banhart, F.; Sun, L. Electron beam etching of CaO crystals observed atom by atom. *Nano Lett.* **2017**, *17*, 5119–5125.
- (8) Di Valentin, C.; Ferullo, R.; Binda, R.; Pacchioni, G. Oxygen vacancies and peroxy groups on regular and low-coordinated sites of MgO, CaO, SrO, and BaO surfaces. *Surf. Sci.* **2006**, *600*, 1147–1154.
- (9) Ménétrey, M.; Markovits, A.; Minot, C.; Pacchioni, G. Formation of Schottky defects at the surface of MgO, TiO₂, and SnO₂: A comparative density functional theoretical study. *J. Phys. Chem. B* **2004**, *108*, 12858–12864.
- (10) Ojamäe, L.; Pisani, C. Theoretical characterization of divacancies at the surface and in bulk MgO. *J. Chem. Phys.* **1998**, *109*, 10984–10995.
- (11) Antoshchenkova, E.; Hayoun, M.; Geneste, G.; Finocchi, F. Thermodynamics and kinetics of the Schottky defect at terraces and steps on the MgO(001) surface. *Phys. Chem. Chem. Phys.* **2010**, *12*, 7251–7257.
- (12) Pacchioni, G.; Pescarmona, P. Structure and stability of oxygen vacancies on sub-surface, terraces, and low-coordinated surface sites of MgO: an ab initio study. *Surf. Sci.* **1998**, *412-413*, 657–671.
- (13) Ferrari, A. M.; Pacchioni, G. Electronic structure of F and V Centers on the MgO surface. *J. Phys. Chem.* **1995**, *99*, 17010–17018.
- (14) Richter, N. A.; Siculo, S.; Levchenko, S. V.; Sauer, J.; Scheffler, M. Concentration of vacancies at metal-oxide surfaces: Case study of MgO(100). *Phys. Rev. Lett.* **2013**, *111*, 045502.
- (15) Alvim, R. d. S.; Borges, L., Jr.; Leitão, A. A. Proton migration on perfect, vacant, and doped MgO(001) surfaces: role of dissociation residual groups. *J. Phys. Chem. C* **2018**, *122*, 21841–21853.
- (16) Geneste, G.; Morillo, J.; Finocchi, F. Adsorption and diffusion of Mg, O, and O₂ on the MgO(001) flat surface. *J. Chem. Phys.* **2005**, *122*, 174707.
- (17) Almeida, A. L.; Martins, J. B. L.; Longo, E.; Furtado, N. C.; Taft, C. A.; Sambrano, J. R.; Lester, W. A., Jr. Theoretical study of MgO(001) surfaces: Pure, doped with Fe, Ca, and Al, and with and without adsorbed water. *Int. J. Quantum Chem.* **2001**, *84*, 705–713.
- (18) Costa, D.; Chizallet, C.; Ealet, B.; Goniakowski, J.; Finocchi, F. Water on extended and point defects at MgO surfaces. *J. Chem. Phys.* **2006**, *125*, 054702.
- (19) Uchino, T.; Yoko, T. Spin-polarized ground states and ferromagnetic order induced by low-coordinated surface atoms and defects in nanoscale magnesium oxide. *Phys. Rev. B: Condens. Matter Mater. Phys.* **2013**, *87*, 144414.
- (20) Mulroue, J.; Duffy, D. M. An ab initio study of the effect of charge localization on oxygen defect formation and migration energies in magnesium oxide. *Proc. R. Soc. A* **2011**, *467*, 2054–2065.
- (21) Kresse, G.; Hafner, J. Ab initio molecular-dynamics simulation of the liquid-metal-amorphous-semiconductor transition in germanium. *Phys. Rev. B: Condens. Matter Mater. Phys.* **1994**, *49*, 14251–14269.
- (22) Kresse, G.; Furthmüller, J. Efficiency of ab-initio total energy calculations for metals and semiconductors using a plane-wave basis set. *Comput. Mater. Sci.* **1996**, *6*, 15–50.
- (23) Kresse, G.; Furthmüller, J. Efficient iterative schemes for ab initio total-energy calculations using a plane-wave basis set. Efficient iterative schemes for ab initio total-energy calculations using a plane-wave basis set. *Phys. Rev. B: Condens. Matter Mater. Phys.* **1996**, *54*, 11169–11186.
- (24) Blöchl, P. E. Projector augmented-wave method. *Phys. Rev. B: Condens. Matter Mater. Phys.* **1994**, *50*, 17953–17979.
- (25) Kresse, G.; Joubert, D. From ultrasoft pseudopotentials to the projector augmented-wave method. *Phys. Rev. B: Condens. Matter Mater. Phys.* **1999**, *59*, 1758–1775.
- (26) Perdew, J. P.; Burke, K.; Ernzerhof, M. Generalized gradient approximation made simple. *Phys. Rev. Lett.* **1996**, *77*, 3865–3868.
- (27) Monkhorst, H. J.; Pack, J. D. Special points for Brillouin-zone integrations. *Phys. Rev. B: Condens. Matter Mater. Phys.* **1976**, *13*, 5188–5192.
- (28) Bader, R. F. W. *Atoms in molecules: A quantum theory*; Oxford University Press: Oxford, U.K., 1990.
- (29) Henkelman, G.; Arnaldsson, A.; Jónsson, H. A fast and robust algorithm for Bader decomposition of charge density. *Comput. Mater. Sci.* **2006**, *36*, 254–360.
- (30) Sanville, E.; Kenny, S. D.; Smith, R.; Henkelman, G. Improved grid-based algorithm for Bader charge allocation. *J. Comput. Chem.* **2007**, *28*, 899–908.
- (31) Tang, W.; Sanville, E.; Henkelman, G. A grid-based Bader analysis algorithm without lattice bias. *J. Phys.: Condens. Matter* **2009**, *21*, 084204.
- (32) Yu, M.; Trinkle, D. R. Accurate and efficient algorithm for Bader charge integration. *J. Chem. Phys.* **2011**, *134*, 064111.
- (33) van de Walle, C. G.; Neugebauer, J. First-principles calculations for defects and impurities: Applications to III-nitrides. *J. Appl. Phys.* **2004**, *95*, 3851–3879.
- (34) Lee, J.; Han, S. Thermodynamics of native point defects in α -Fe₂O₃: an ab initio study. *Phys. Chem. Chem. Phys.* **2013**, *15*, 18906–18914.
- (35) Smith, D. K.; Leider, H. R. Low-temperature thermal expansion of LiH, MgO and CaO. *J. Appl. Crystallogr.* **1968**, *1*, 246–249.
- (36) Brudevoll, T.; Kotomin, E. A.; Christensen, N. E. Interstitial-oxygen-atom diffusion in MgO. *Phys. Rev. B: Condens. Matter Mater. Phys.* **1996**, *53*, 7731–7735.
- (37) Robach, O.; Renaud, G.; Barbier, A. Very-high-quality MgO(001) surfaces: roughness, rumpling and relaxation. *Surf. Sci.* **1998**, *401*, 227–235.
- (38) Gerson, A. R.; Bredow, T. MgO(100) surface relaxation and vacancy defects: a semi-empirical quantum-chemical study. *Phys. Chem. Chem. Phys.* **1999**, *1*, 4889–4896.
- (39) Sushko, P. V.; Shluger, A. L.; Catlow, C. R. A. Relative energies of surface and defect states: ab initio calculations for the MgO(001) surface. *Surf. Sci.* **2000**, *450*, 153–170.
- (40) Baumeier, B.; Krüger, P.; Pollmann, J. Bulk and surface electronic structures of alkaline-earth metal oxides: Bound surface and image-potential states from first principles. *Phys. Rev. B: Condens. Matter Mater. Phys.* **2007**, *76*, 205404.
- (41) Gilbert, C. A.; Kenny, S. D.; Smith, R.; Sanville, E. Ab initio study of point defects in magnesium oxide. *Phys. Rev. B: Condens. Matter Mater. Phys.* **2007**, *76*, 184103.
- (42) Uberuaga, B. P.; Smith, R.; Cleave, A. R.; Henkelman, G.; Grimes, R. W.; Voter, A. F.; Sickafus, K. E. Dynamical simulations of radiation damage and defect mobility in MgO. *Phys. Rev. B: Condens. Matter Mater. Phys.* **2005**, *71*, 104102.
- (43) Henkelman, G.; Uberuaga, B. P.; Harris, D. J.; Harding, J. H.; Allan, N. L. MgO addimer diffusion on MgO(100): A comparison of

ab initio and empirical models. *Phys. Rev. B: Condens. Matter Mater. Phys.* **2005**, *72*, 115437.

(44) Kantorovich, L. N.; Holender, J. M.; Gillan, M. J. The energetics and electronic structure of defective and irregular surfaces on MgO. *Surf. Sci.* **1995**, *343*, 221–239.

(45) Schönberger, U.; Aryasetiawan, F. Bulk and surface electronic structures of MgO. *Phys. Rev. B: Condens. Matter Mater. Phys.* **1995**, *52*, 8788–8793.

(46) Henrich, V. E.; Dresselhaus, G.; Zeiger, H. J. Energy-dependent electron-energy-loss spectroscopy: Application to the surface and bulk electronic structure of MgO. *Phys. Rev. B: Condens. Matter Mater. Phys.* **1980**, *22*, 4764–4775.

(47) Cox, P. A.; Williams, A. A. Surface excitons on ionic crystals. *Surf. Sci.* **1986**, *175*, L782–L786.

(48) Momma, K.; Izumi, F. VESTA 3 for three-dimensional visualization of crystal, volumetric and morphology data. *J. Appl. Crystallogr.* **2011**, *44*, 1272–1276.